# Effect of horizontal aspect ratio on magnetoconvective instabilities in liquid metals

Lekha Sharma [*]
*Department of Mathematics, National Institute of Technology, Durgapur 713209, India*

Manojit Ghosh [†]
*Engineering Mechanics Unit, Jawaharlal Nehru Centre for Advanced Scientific Research, Jakkur P.O., Bangalore 560064, India*

Pinaki Pal [‡]
*Department of Mathematics, National Institute of Technology, Durgapur 713209, India*

(Received 24 October 2021; accepted 1 February 2022; published 14 February 2022)

Three-dimensional direct numerical simulations (DNS) are performed to uncover the effect of the horizontal aspect ratio ($\Gamma = k_y/k_x$, $k_x$ and $k_y$ being the wave numbers along the $x$ and $y$ directions, respectively) on magnetoconvective instabilities using plane layer Rayleigh-Bénard geometry in the presence of an external uniform horizontal magnetic field. The fluid under consideration is an electrically conducting, Newtonian fluid (liquid metal) having a very small Prandtl number ($\mathrm{Pr} \sim 10^{-2}$) and vanishingly small magnetic Prandtl number ($\mathrm{Pm} \sim 10^{-6}$). Extensive DNS are conducted to explore the dynamics of the system by varying the control parameters, namely, the Chandrasekhar number ($Q$, strength of the magnetic field) and the Rayleigh number (Ra, vigor of the buoyancy) together with $\Gamma$ in the ranges of $0 < Q \leqslant 10^3$, $0 < \mathrm{Ra} \leqslant 7 \times 10^3$, and $1/2 \leqslant \Gamma \leqslant 6$. It is found that both $Q$ and $\Gamma$ have a similar effect on the system dynamics in the sense that an increment in either of them delays the oscillatory instability and enhances the stability regime of two-dimensional rolls. The onset of oscillatory instability is found to scale as $Q^{\alpha}$. Two different scaling exponents have been identified depending on the strength of the magnetic field and $\Gamma$. For weak and moderate magnetic field ($Q < 100$), the exponent $\alpha$ is found to be much higher compared to that of a stronger magnetic field ($Q \geqslant 100$) and gradually decreases with the increment in $\Gamma$. Different routes to chaos are also observed depending on $\Gamma$ and $Q$ including the well-known period doubling and quasiperiodic routes to chaos. The appearance of transient chaos (TC) in the system due to the presence of chaotic saddles is found to be a remarkable finding of the present study. It is found that TC eventually leads to persistent chaos and can be considered as a possible route to chaos in magnetoconvection. Chaotic flow reversals induced by an attractor-merging crisis are also observed for $\Gamma \leqslant 3$. Interestingly, we notice transient chaotic flow reversals in a wide parameter space which may be attributed to the presence of a merged chaotic saddle there. It is found that transient chaotic flow reversals also lead to persistent chaotic flow reversals as the Rayleigh number increases.

DOI: 10.1103/PhysRevFluids.7.023502

[*]lekhasharma27@gmail.com
[†]manojitmath@gmail.com
[‡]pinaki.pal@maths.nitdgp.ac.in

 

## I. INTRODUCTION

The convective motion of an electrically conducting fluid in the presence of a magnetic field, generally referred to as magnetoconvection (MC), has always fascinated researchers due to its relevance to various astrophysical and industrial applications. For example, MC is considered to play a major role in the formation of sunspots, solar granulation, and generation of magnetic field in stars, planets, moons, and asteroids [1–3]. Apart from these examples, MC also has a significant influence on several industrial processes such as crystal growth, nuclear heat exchangers, and the vacuum arc remelting (VAR) refining process [4–6]. Thus, understanding the dynamics of these systems is of utmost importance. However, the arbitrary geometry, remoteness, and other complexities do not allow direct investigation of these systems. Therefore, generic models are used to study these systems both experimentally and theoretically. The convective motion of a fluid between two horizontal plates driven by an unstable temperature gradient, classically known as the Rayleigh-Bénard convection (RBC), is one such generic model which allows one to study the above mentioned systems in their simplest form [7–9]. If the working fluid is electrically conducting, then RBC in the presence of a magnetic field provides a fundamental model for MC, generally referred as Rayleigh-Bénard magnetoconvection (RBM) [10,11]. The dynamics of RBM is controlled by four dimensionless parameters: the Rayleigh number (Ra, measures the buoyancy force), the Chandrasekhar number ($Q$, measures the strength of the magnetic field), the Prandtl number (Pr, ratio of kinematic viscosity and thermal diffusivity of the fluid), and the magnetic Prandtl number (Pm, ratio of kinematic viscosity and magnetic diffusivity of the fluid). In the case of confined geometry, the aspect ratios (vertical and horizontal) of the fluid vessel are also found to affect the system dynamics and are considered as extra parameters.

The linear stability analysis of RBM assuming an infinite fluid layer reveals that the presence of a horizontal magnetic field does not affect the critical Rayleigh number ($\mathrm{Ra_c}$) for the onset of convection, and it is independent of both $Q$ and Pr [10]. However, the presence of a horizontal magnetic field increases the region of stable two-dimensional (2D) rolls, which delays the onset of oscillatory instability [12]. The onset of oscillatory instability is found to scale with the strength of the magnetic field as $Q^{\alpha}$ with $\alpha = 1.2$ [12]. Such a scaling was also observed in the experiments conducted in mercury by Fauve *et al.* [13]. However, the exponent $\alpha = 1.2$ does not seem to be universal as boundary conditions, and aspect ratios have a strong influence on it [13–15]. It is well known that for low-Pr fluids (liquid metals), transition to the three-dimensional (3D) time-dependent convection occurs very near the convection threshold due to the generation of vertical vorticity [16]. The presence of a horizontal magnetic field suppresses the 3D time-dependent convection and manifests 2D steady convection [17,18]. This causes an increment in Nusselt number (Nu) before oscillatory convection sets in [17–19]. Apart from the oscillatory instability, another interesting aspect is to investigate the development of chaotic flow with the increment in Ra corresponding to different $Q$. Experiments conducted with low-Pr fluids exhibit two different routes to chaos depending on the strength of the magnetic field [20]. The period doubling route to chaos is observed for low $Q$, while the quasiperiodic route to chaos is found for higher $Q$ [20]. A detailed numerical investigation, including bifurcation analysis by Nandukumar and Pal, also supports these findings [14]. The intermittent route to chaos is also observed in a low-dimensional model of RBM [21]. It is found that low-Pr fluids also exhibit flow reversals very near the convection threshold and the presence of a horizontal magnetic field has a strong influence on it [22–24]. Understanding the dynamics of flow reversals is fundamental due to its occurrence in geophysical and industrial applications [6,25]. Experimental and numerical studies with liquid gallium in the presence of a horizontal magnetic field reveals that flow reversals occur in confined RBM due to the coupling of large-scale horizontal circulations and fluctuations present in the convection rolls, which induce bending and reconnection of rolls [23,26]. More recently, Ghosh *et al.* performed the numerical analysis of RBM assuming an infinite fluid layer and established presence of an attractor-merging crisis in higher dimensional phase space which is found to cause the flow reversals [24]. It is also

found that an increment in strength of the magnetic field delays the flow reversals phenomena until higher Ra [24].

The present study is a substantial extension of the previous studies by Nandukumar and Pal [14] and Ghosh *et al.* [24]. We have varied the horizontal aspect ratio ($\Gamma = k_y/k_x$, $k_x$ and $k_y$ being the wave numbers along the $x$ and $y$ directions, respectively) of the simulation box to explore its effect on the system dynamics. We have carried out extensive direct numerical simulations (DNS) of the hydromagnetic system with stress-free electrically conducting boundaries in a 3D simulation box of size $2\pi/k_x \times 2\pi/k_y \times 1$ for wide range of $Q$ ($0 < Q \leqslant 10^3$) and $\Gamma$ ($1/2 \leqslant \Gamma \leqslant 6$) for this purpose. We found two different scalings for the onset of oscillatory instability depending on the strength of the magnetic field. Standard routes to chaos, including the well-known period doubling and quasiperiodic routes, are also observed depending on $Q$ and $\Gamma$. The heat transport properties associated with these solutions are also explored in detail. Interestingly, we noticed the presence of transient chaos and transient chaotic flow reversals in the system, which are eventually found to lead to persistent chaos and persistent chaotic flow reversals.

The rest of the paper is arranged as follows. In Sec. II we present the mathematical framework of the physical system under consideration. Section III describes the numerical technique used to solve the governing equations. Section IV is dedicated to the results, and some conclusive remarks are drawn in Sec. V.

## II. PHYSICAL SYSTEM AND GOVERNING EQUATIONS

The physical system consists of a classical Rayleigh-Bénard geometry in which an infinitely extended thin horizontal layer of homogeneous, electrically conducting, Newtonian fluid is confined between two parallel plates subjected to an external uniform horizontal magnetic field $\mathbf{B}_0 = (0, B_0, 0)$. Both plates are assumed to be perfect conductors of heat and electricity. The lower plate is heated uniformly, and the upper plate is cooled to maintain a steady temperature gradient $\beta = \Delta T/d = (T_l - T_u)/d$ across the fluid layer. $T_l$ and $T_u$ are, respectively, the temperature of the lower and upper plate with $T_l > T_u$ and $d$ being the thickness of the fluid layer. We assume the validity of the Boussinesq approximation, i.e., the density of the fluid ($\rho$) under consideration varies linearly with the temperature and the fluid is treated as an incompressible one [27]. The base state is then the trivial conduction state characterized by

$$T_b(z) = T_l - \beta z,\ \rho_b(z) = \rho_l(1 + \alpha\beta z),\ \text{and}\ P_b(z) = P_l - g\rho_l\left(z + \frac{1}{2}\alpha\beta z^2\right) - \frac{|\mathbf{B_0}|^2}{2\mu_0}. \tag{1}$$

In the above equation, $T_l$, $\rho_l$, and $P_l$, respectively, represent the temperature, density, and pressure of the fluid at the lower boundary. The coefficients $\alpha$, $\mu_0$, and $g$ are, respectively, the coefficient of volume expansion of the fluid, permeability of free space, and acceleration due to gravity. As the temperature difference $\Delta T$ crosses a critical value, convection sets in and the base state becomes slightly perturbed. The convective motion of the fluid is then governed by the following set of dimensionless equations:

$$\frac{\mathcal{D}\mathbf{v}}{\mathcal{D}t} - Q\left[\frac{\partial \mathbf{b}}{\partial y} + \mathrm{Pm}(\mathbf{b}\cdot\nabla)\mathbf{b}\right] = -\nabla p + \mathrm{Ra}\theta\hat{\mathbf{e}}_3 + \nabla^2\mathbf{v}, \tag{2}$$

$$\mathrm{Pm}\left[\frac{\mathcal{D}\mathbf{b}}{\mathcal{D}t} - (\mathbf{b}\cdot\nabla)\mathbf{v}\right] = \nabla^2\mathbf{b} + \frac{\partial \mathbf{v}}{\partial y}, \tag{3}$$

$$\mathrm{Pr}\frac{\mathcal{D}\theta}{\mathcal{D}t} = v_3 + \nabla^2\theta, \tag{4}$$

$$\nabla\cdot\mathbf{v} = 0, \quad \text{and} \quad \nabla\cdot\mathbf{b} = 0. \tag{5}$$

In Eqs. (2)–(5), $\mathcal{D}/\mathcal{D}t = \partial/\partial t + (\mathbf{v}\cdot\nabla)$ is the convective derivative, $\mathbf{v} = (v_1, v_2, v_3)$ is the perturbed or convective velocity field, $\mathbf{b} = (b_1, b_2, b_3)$ is the induced magnetic field, $\theta$ represents the deviation of temperature from base state, $p$ is the perturbation of pressure, and $\hat{\mathbf{e}}_3$ is the unit

vector acting vertically upwards opposite to gravity. These equations are made dimensionless using $d$ as the length scale, viscous diffusion time $d^2/\nu$ ($\nu$ being the kinematic viscosity of the fluid) as the timescale, $\nu/d$ as the velocity scale, $\Delta T\nu/\kappa$ ($\kappa$ being the thermal diffusivity of the fluid) as the temperature scale, and $B_0\nu/\lambda$ ($\lambda$ being the magnetic diffusivity of the fluid) as the scale for the magnetic field. The nondimensionalization procedure gives rise to four dimensionless parameters which control the dynamics of the system: the Rayleigh number $\mathrm{Ra} = \alpha g \Delta T d^3/\nu\kappa$, the Chandrasekhar number $Q = B_0^2 d^2/\mu_0 \rho_l \nu\lambda$, the Prandtl number $\mathrm{Pr} = \nu/\kappa$, and the magnetic Prandtl number $\mathrm{Pm} = \nu/\lambda$. We consider low-Prandtl number fluids ($\mathrm{Pr} \sim 10^{-2}$) such as liquid metals to carry out our investigation. For these fluids, the magnetic diffusion timescale is the shortest one compared to the other timescales [17]. As a result, the induced magnetic field $\mathbf{b}$ which is generated due to the fluid motion is much smaller than the external magnetic field $\mathbf{B}_0$ and adjusts instantaneously to the time dependence of the velocity field [28]. Therefore, we adopt the quasi-static approximation $\mathrm{Pm} \to 0$ [29]. Equations (2) and (3) in the vicinity of this limit reduce to

$$\frac{\mathcal{D}\mathbf{v}}{\mathcal{D}t} - Q\frac{\partial \mathbf{b}}{\partial y} = -\nabla p + \mathrm{Ra}\theta\hat{\mathbf{e}}_3 + \nabla^2\mathbf{v}, \tag{6}$$

$$\nabla^2\mathbf{b} = -\frac{\partial \mathbf{v}}{\partial y}. \tag{7}$$

The bounding plates are assumed to be stress-free, which gives the boundary conditions for the velocity field

$$v_3 = \frac{\partial v_1}{\partial z} = \frac{\partial v_2}{\partial z} = 0 \quad \text{at} \quad z = 0, 1. \tag{8}$$

The boundary conditions for $\theta$ and $\mathbf{b}$ arise from the fact that both bounding plates are perfect conductors of heat and electricity, which gives

$$\theta = b_3 = \frac{\partial b_1}{\partial z} = \frac{\partial b_2}{\partial z} = 0 \quad \text{at} \quad z = 0, 1. \tag{9}$$

Therefore, Eqs. (4)–(7) together with the boundary conditions (8) and (9) provide the complete mathematical framework to study the above mentioned physical system. The results from linear stability analysis of the system are well known; i.e., the stationary convection onset is independent of both Pr and $Q$ [11,17]. Thus, the critical Rayleigh number ($\mathrm{Ra_c} = 27\pi^4/4$) and associated wave number ($k_c = \pi/\sqrt{2}$) are not different from the nonmagnetic case. However, both Pr and $Q$ as well as geometry of the system have a strong influence on the higher order instabilities when nonlinearities are taken into account. To explore this, we perform direct numerical simulations (DNS) of the governing equations by varying the horizontal aspect ratio ($\Gamma$) of the simulation box, details of which are discussed in Sec. III.

## III. DIRECT NUMERICAL SIMULATIONS (DNS)

An open-source pseudospectral code Tarang [30] is used to perform 3D DNS of the governing equations (4)–(7) together with the boundary conditions (8) and (9). In the simulation code velocity components and temperature are expanded in terms of orthogonal basis functions compatible with the boundary conditions. Therefore, in the code the expressions for $v_1$, $v_2$, $v_3$, and $\theta$ read as

$$\begin{aligned}(v_1, v_2) &= \sum_{l,m,n} (U_{lmn}(t), V_{lmn}(t)) e^{i(lk_x x + mk_y y)} \cos(n\pi z), \\ (v_3, \theta) &= \sum_{l,m,n} (W_{lmn}(t), T_{lmn}(t)) e^{i(lk_x x + mk_y y)} \sin(n\pi z).\end{aligned} \tag{10}$$

In expression (10), $U_{lmn}$, $V_{lmn}$, $W_{lmn}$, and $T_{lmn}$ are the Fourier modes with $l$, $m$, and $n$ being the non-negative integers. Simulations are carried out in a rectangular box of size $2\pi/k_x \times 2\pi/k_y \times 1$ with $k_x$ and $k_y$ being the wave numbers along the $x$ and $y$ directions, respectively. Periodicity is assumed in the horizontal directions to idealize the infinitely extended fluid layer. The horizontal aspect ratio of the simulation box is then defined as $\Gamma = k_y/k_x$. Thus, $\Gamma > 1$ indicates contraction of the simulation box in the $y$ direction, while $\Gamma < 1$ implies expansion of the box in the $y$ direction without affecting the box in the $x$ direction. We perform simulations by varying $\Gamma$ in the range $1/2 \leqslant \Gamma \leqslant 6$. We set $k_x = k_c$ and vary $k_y$ in the range $k_c/2 \leqslant k_y \leqslant 6k_c$. Note that variation in $\Gamma$ does not influence $\mathrm{Ra}_c$ and $k_c$. We consider maximum $64^3$ grid resolution, while most simulations are performed with $32^3$. Time advancement is done with the fourth-order Runge-Kutta method with Courant-Friedrichs-Lewy condition. To describe the results lucidly, we introduce a parameter $r = \mathrm{Ra}/\mathrm{Ra_c}$ in the subsequent discussions, called the reduced Rayleigh number. Therefore, at $r = 1$ convection sets in.

## IV. RESULTS

We perform DNS in a widespread parameter space by varying $\Gamma$ and $Q$ in the ranges of $1/2 \leqslant \Gamma \leqslant 6$ and $0 < Q \leqslant 1000$ corresponding to $\mathrm{Pr} = 0.025$. We focus on the dynamics of the system that appear near the onset ($r \leqslant 10$) and explore several aspects of it, including the oscillatory instability, transition to chaos, heat transport properties, and flow reversals. These aspects are discussed in the following subsections.

### A. The oscillatory instability

One of the interesting features of low-Pr convection is the oscillatory instability (OI) of rolls, which occurs as Ra crosses a critical value after convection sets in [16]. In this process, steady 2D rolls lose stability due to the generation of vertical vorticity, and 3D time-dependent flow emerges in the form of standing or traveling waves. It is found that the presence of a horizontal magnetic field inhibits the OI and postpones it to the higher Ra following a well-defined power law $(\mathrm{Ra_Q}^{(O)} - \mathrm{Ra_0}^{(O)}) \propto Q^{\alpha}$ where $\mathrm{Ra_Q}^{(O)}$ and $\mathrm{Ra_0}^{(O)}$, respectively, represent the OI onset for given $Q$

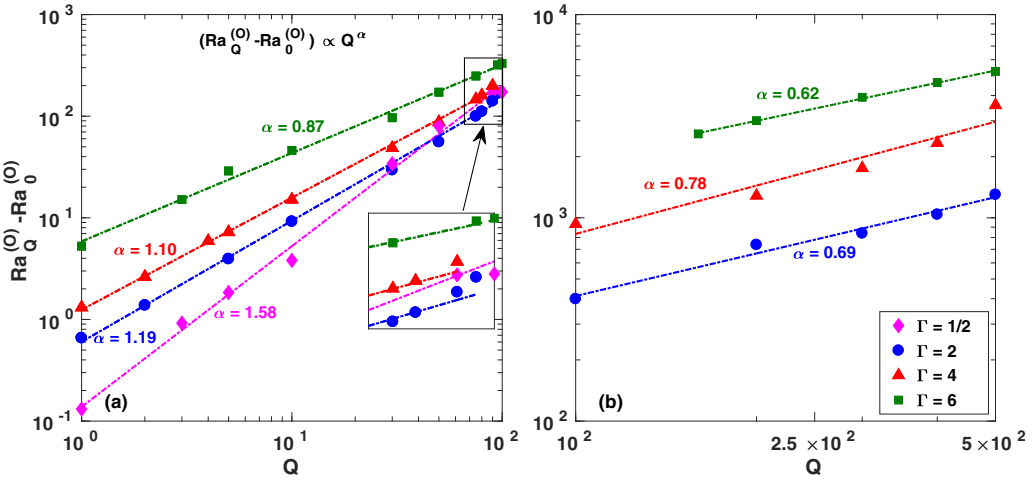


FIG. 1. Scaling of the oscillatory instability onset with $Q$ corresponding to different $\Gamma$: (a) for weak and moderate magnetic field ($0 < Q < 100$), and (b) for a stronger magnetic field ($100 \leqslant Q \leqslant 500$). Magenta diamonds, blue circles, red triangles, and green squares, respectively, represent the data for $\Gamma = 1/2$, 2, 4, and 6. The dash-dot lines denote their best fit. A zoomed view of (a) is shown at the inset.

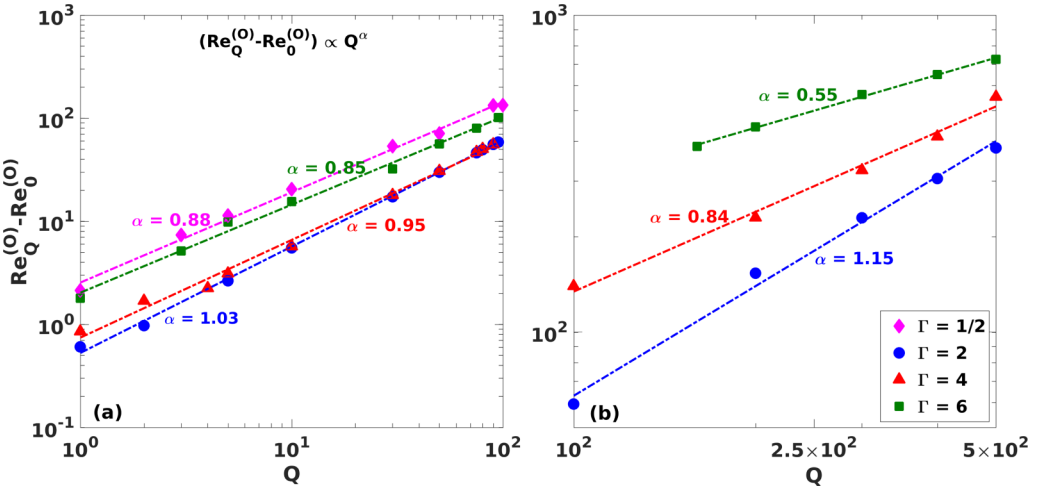


FIG. 2. Variation of $(Re_Q{}^{(O)} - Re_0{}^{(O)})$ as a function of $Q$ corresponding to different $\Gamma$: (a) for a weak and moderate magnetic field ($0 < Q < 100$), and (b) for a stronger magnetic field ($100 \leqslant Q \leqslant 500$). The color coding and line style are same as in Fig. 1.

($\neq 0$) and $Q = 0$ [12,13]. Now, to unfold the effect of aspect ratio on the OI onset in the presence of a horizontal magnetic field, we perform DNS by varying both $\Gamma$ and $Q$. We first observe that the onset of convection ($r = 1$) is independent of $Q$ for all values of $\Gamma$, and steady 2D rolls aligned along the $y$ axis prevail there. At large $\Gamma$ ($\Gamma > 1$), the orientation of rolls, aligned along the y-axis is found to be consistent with the experimental findings of Stork and Müller as the $y$ direction of the simulation box is shorter [31]. On the other hand, at small $\Gamma$ ($\Gamma < 1$), the rolls are aligned along the $y$ axis due to the presence of magnetic field in that direction. Now, as we increase the value of $r$, 2D rolls become unstable depending on $\Gamma$ and $Q$, and the OI emerges in the form of a standing wave. The appearance of a vanishingly small-amplitude limit cycle with finite frequency also ensures the existence of a supercritical Hopf bifurcation there. The effect of $\Gamma$ on OI is shown in Fig. 1. In the figure, variation of $(Ra_Q{}^{(O)} - Ra_0{}^{(O)})$ is displayed as a function of $Q$ corresponding to different $\Gamma$. Interestingly, it is found that for different $\Gamma$, $(Ra_Q{}^{(O)} - Ra_0{}^{(O)})$ scales as $Q^\alpha$ with two distinct values of $\alpha$ depending on the strength of the magnetic field. For relatively weak magnetic field ($Q < 100$), the value of $\alpha$ is found to be higher compared to the case of stronger magnetic field ($100 \leqslant Q \leqslant 500$). In other words, for fixed $\Gamma$, a stronger magnetic field is found to have more inhibition power compared to a weaker one. Figure 1 also illustrates that at fixed $Q$, increasing $\Gamma$ delays the OI onset as $r$ increases, just as increasing $Q$ at fixed $\Gamma$ delays the OI onset with $r$. The values of $\alpha$ for $\Gamma = 2$ and 4 obtained in the present study show a close match with the experimental findings of Fauve *et al.* [13]. However, the experiments involved only two aspect ratios ($\Gamma = L_x/L_y = 4$ and $\approx 2$); the delay of the OI onset when $Q$ is increased is smaller when the aspect ratio is smaller. The present study also reveals the same result. The small deviation in $\alpha$ arises due to the difference in the boundary conditions which have a strong influence on the OI. For stress-free boundaries, the OI occurs at zero wave number in contrast to the case of rigid boundaries, where it takes place at a finite wave number [16,32]. Moreover, for stress-free boundaries, the OI tends to the onset of convection ($r = 1$) as $\mathrm{Pr} \to 0$, while it stays at a finite value above the convection threshold ($r > 1$) in the case of rigid boundaries. This is related to the externally broken Galilean invariance in the case of rigid boundary conditions [33]. Therefore, it is surprising that a reasonably good agreement is observed between simulations and experiments. This may result from the small extension along the perpendicular axis of the rolls considered in the simulations that limits the wavelength of the oscillatory instability.

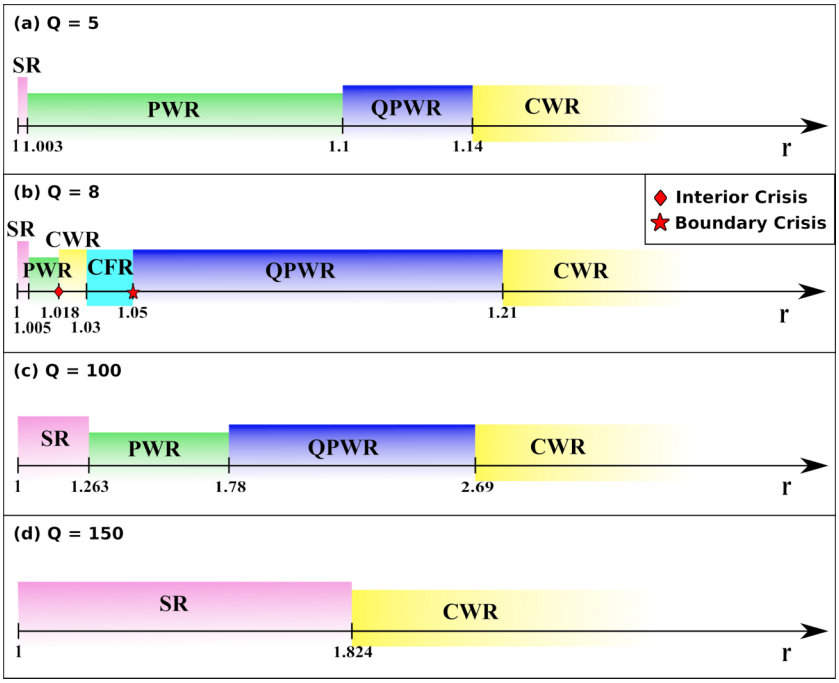


FIG. 3. Line bifurcation diagrams obtained from DNS for $\Gamma = 1/2$ corresponding to four $Q$: (a) $Q = 5$, (b) $Q = 8$, (c) $Q = 100$, and (d) $Q = 150$. Magenta, green, blue, and yellow patches, respectively, represent the regions of steady 2D rolls (SR), periodic wavy rolls (PWR), quasiperiodic wavy rolls (QPWR), and chaotic wavy rolls (CWR). The cyan region in (b) denotes the parameter space where chaotic flow reversals (CFR) occur, while the red diamond and star denote the interior and boundary crises points.

To check the universality of coefficient $\alpha$, we further calculate the Reynolds number (Re) at the OI onset defined as $\mathrm{Re} = Vd/\nu$, $V$ being the velocity of 2D rolls. The variation of $(\mathrm{Re_Q}^{(O)} - \mathrm{Re_0}^{(O)})$ as a function of $Q$ corresponding to different $\Gamma$ is displayed in Fig. 2; $\mathrm{Re_Q}^{(O)}$ and $\mathrm{Re_0}^{(O)}$, respectively, represent the Reynolds number for the OI onset for a given $Q$ ($\neq 0$) and $Q = 0$. From Fig. 2 it is evident that for a weak and moderate magnetic field, $(\mathrm{Re_Q}^{(O)} - \mathrm{Re_0}^{(O)})$ scales as $Q^{\alpha}$ with $\alpha \sim 1$ for all $\Gamma$. This is found to be in good agreement with the argument given in Ref. [13]. On the other hand, the value of $\alpha$ is found to decay with the increment in $\Gamma$ corresponding to a stronger magnetic field [Fig. 2(b)]. Note that, for $\Gamma = 1/2$, we notice a sharp transition to chaos from steady 2D rolls for $Q > 130$. As a result, the OI does not appear corresponding to these parameter values.

From the above discussion, it is evident that $\Gamma$ has strong influence on the flow dynamics of the system, and we explore it further by investigating the subsequent OI transitions to chaos, which is discussed in Sec. IV B.

### B. Transition to chaos

#### *1. Aspect ratio,* $\Gamma = 1/2$

The evolution of oscillatory instability to the chaos in RBM of low-Pr fluids is found to be a fascinating yet complex process [14,34]. Depending on the strength of the magnetic field, two well-known routes have been documented in the literature, namely, the period doubling route to chaos and quasiperiodic route to chaos. Experimental [20,35] and numerical studies [14] reveal that the period doubling route to chaos is observed for a relatively weak magnetic field, while a moderate or strong magnetic field favors the quasiperiodic route to chaos. To explore the effect of aspect ratio

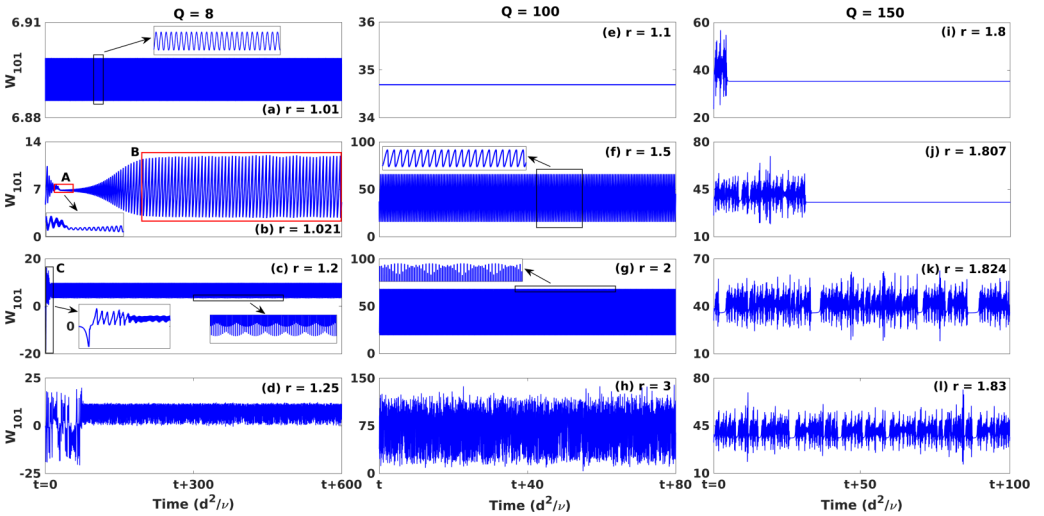


FIG. 4. Time series of the dominant Fourier mode $W_{101}$ corresponding to three $Q$ illustrating transitions to chaos for $\Gamma = 1/2$. The left (a–d), middle (e–h), and right (i–l) columns, respectively, correspond to $Q = 8$, 100, and 150. The insets in (a), (b), (c), (f), and (g) show the zoomed view of the corresponding selections.

on these routes, we perform extensive DNS by varying $r$ corresponding to given $\Gamma$ and $Q$. We start with $\Gamma = 1/2$ and notice two distinct routes to chaos depending on the strength of the magnetic field. For relatively lower $Q$ ($Q \leqslant 130$), where the OI exists, we observe a quasiperiodic route to chaos. Figures 3(a)–3(c) illustrate the scenario for three different $Q$. For $Q = 5$ [Fig. 3(a)] and $Q = 100$ [Fig. 3(c)], we observe that the OI or periodic wavy rolls (PWR) bifurcate into quasiperiodic wavy rolls (QPWR) with the increment in $r$, which finally becomes chaotic wavy rolls (CWR) as $r$ is increased further. The typical time evolution of the largest Fourier mode $W_{101}$ corresponding to these transitions is displayed in Figs. 4(e)–4(h) for $Q = 100$. Note that transition to QPWR in these cases occurs due to the generation of an incommensurate second frequency. On the other hand, we notice a different dynamics in the range $7 \leqslant Q \leqslant 36$ where a chaotic window exists between PWR and QPWR [Fig. 3(b)]. Figures 4(a)–4(d) display the corresponding time series of the dominant Fourier mode $W_{101}$. The appearance of chaos in the interval $1.018 \leqslant r \leqslant 1.05$ may be attributed to an interior crisis at $r = 1.018$ where sudden enhancement of the chaotic attractor takes place [36]. The wide chaotic attractor [B in Fig. 4(b)] and escaping of the trajectory from transient QPWR to CWR is shown in Fig. 4(b). With the increment in $r$, chaotic flow reversals (CFR) appear in the system, which will be discussed in greater detail in Sec. IV D. Now, as $r$ increases further at $r = 1.05$ a boundary crisis occurs [36]. As a result, the chaotic attractor suddenly disappears from the system resulting in chaotic transient and QPWR is observed there [Fig. 4(c)]. Further increment in $r$ once again brings back CWR in the system from QPWR [Fig. 4(d)].

For relatively larger $Q(Q > 130)$, we notice transient chaos in the system where trajectories exhibit finite-time chaotic behavior before settling to the stable 2D rolls. Figures 4(i) and 4(j) depict the scenario for $Q = 150$. The appearance of transient chaos may be attributed to the presence of chaotic saddles or strange saddles in the system. These are nonattracting chaotic sets with the properties of aperiodicity and sensitivity to the initial conditions [37–39]. As a result, neighboring trajectories spend finite time in the vicinity of the chaotic set before converging to some coexisting attractor. Now, as we increase $r$ gradually, the transient trapping time of the trajectories also increases, and we observe the appearance of persistent chaos in the system [Figs. 4(k) and 4(l)]. Therefore, we observe a direct transition to chaos from stable 2D rolls due to the appearance of transient chaos in the system. Note that the appearance of transient chaos in magnetoconvection has been reported earlier by analyzing a low-dimensional model (generalized Lorenz model) [21,37].

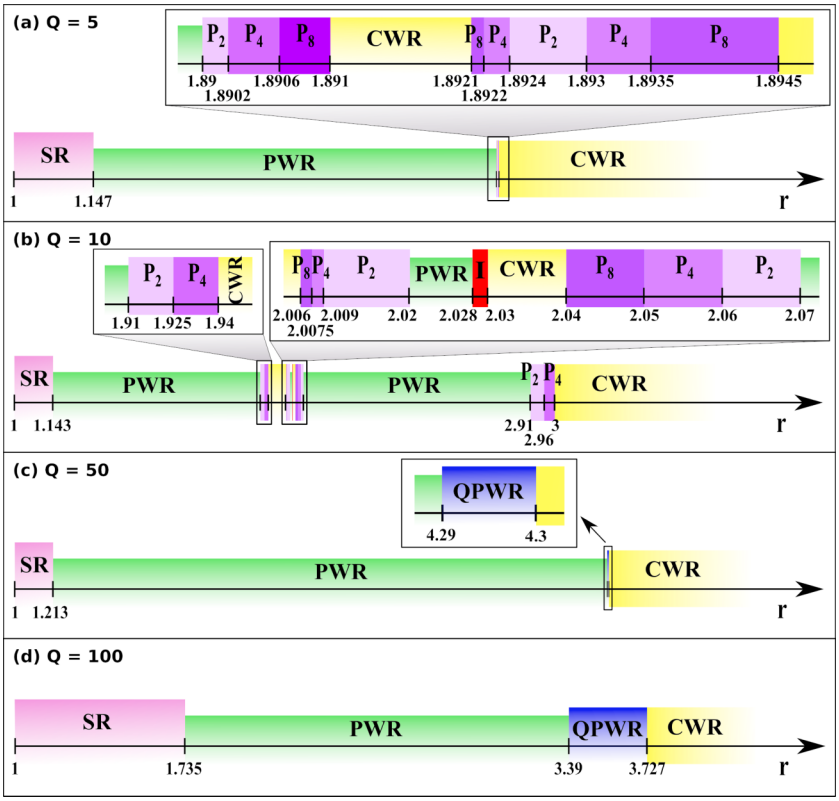


FIG. 5. Line bifurcation diagrams computed from DNS for $\Gamma = 2$ corresponding to four $Q$: (a) $Q = 5$, (b) $Q = 10$, (c) $Q = 50$, and (d) $Q = 100$. The color coding for SR, PWR, QPWR, and CWR is same that has been used in Fig. 3. Light, medium, and dark violet patches represent period 2 ($P_2$), period 4 ($P_4$), and period 8 ($P_8$) solutions, respectively. The region of the intermittent (I) solution is shown in red. Zoomed views of forward and inverse period doubling cascades are shown in (a) and (b), while an enlarged view of QPWR is shown in (c).

Here we show that it is a possible route to persistent chaos in the quasi-static magnetoconvection as system geometry is varied.

### *2. Aspect ratio,* $\Gamma = 2$

The route to chaos for $\Gamma = 1$ has already been explored in detail by Nandukumar and Pal [14]. For lower $Q$ they found period doubling route to chaos, while the quasiperiodic route is observed for higher $Q$. Now we turn our attention to $\Gamma = 2$. Figure 5 summarizes the findings where different flow states bifurcate from PWR together with their successive transitions to chaos corresponding to four different $Q$. We observe a period doubling cascade for lower $Q$ and a quasiperiodic route to chaos for moderate and higher $Q$. However, the dynamics associated with the period doubling cascade for lower $Q$ is found to be much more complex [see Figs. 5(a) and 5(b)]. For very low $Q$ ($Q = 5$), we notice a forward period doubling cascade which leads to CWR occurring in a very narrow regime, i.e., PWR $\rightarrow$ Period 2 ($P_2$) $\rightarrow$ Period 4 ($P_4$) $\rightarrow$ Period 8 ($P_8$) $\rightarrow$ CWR [Fig. 5(a)]. With the increment in $r$, CWR turns into $P_2$ following an inverse doubling cascade (CWR $\rightarrow$ $P_8$ $\rightarrow$ $P_4$ $\rightarrow$ $P_2$), which becomes CWR again via a forward doubling cascade ($P_2$ $\rightarrow$ $P_4$ $\rightarrow$ $P_8$ $\rightarrow$ CWR) as $r$ is increased further. Now, as we increase $Q$ by a small amount, the dynamics of the system changes. For $Q = 10$ we observe occurrence of forward (PWR $\rightarrow$ $P_2$ $\rightarrow$ $P_4$ $\rightarrow$ CWR) and inverse (CWR $\rightarrow$ $P_8$ $\rightarrow$

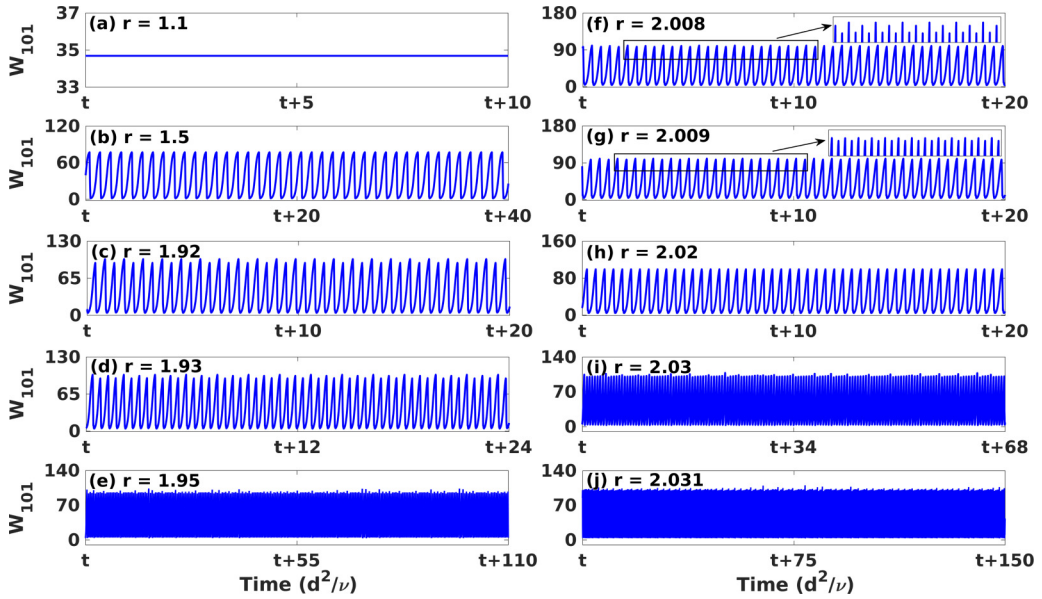


FIG. 6. The time evolution of the largest Fourier mode $W_{101}$ for $\Gamma = 2$ and $Q = 10$. The insets in (f) and (g) show the zoomed view of the corresponding selections.

$P_4 \rightarrow P_2 \rightarrow$ PWR) doubling cascades in quick succession as $r$ is raised [Fig. 5(b)]. The time evolution of the dominant Fourier mode $W_{101}$ corresponding to the forward and inverse cascades is shown in Figs. 6(b)–6(h). Now, as $r$ is raised further, the PWR loses stability and intermittency (I) appears in the system followed by CWR [see Figs. 6(h)–(j)]. Further increment in $r$ brings back PWR again through an inverse doubling cascade (CWR $\rightarrow P_8 \rightarrow P_4 \rightarrow P_2 \rightarrow$ PWR) before it turns into CWR following a forward doubling cascade (PWR $\rightarrow P_2 \rightarrow P_4 \rightarrow$ CWR). For moderate $Q$ ($Q = 50$), we observe that the regimes of 2D rolls and PWR are enhanced [Fig. 5(c)]. The PWR bifurcates to QPWR with the increment in $r$, which further gives rise to CWR. Thus, the route to chaos in this case is standard quasiperiodic route to chaos. Further increment in $Q$ does not bring any qualitative changes in the system [see Fig. 5(d)], and we observe a quasiperiodic route to chaos in a wide range ($40 \leqslant Q \leqslant 1000$).

### *3. Aspect ratio,* $\Gamma = 4$

Next, we consider $\Gamma = 4$. For low $Q$, we observe appearance of PWR and 2D rolls windows in alteration before a sharp transition from 2D rolls to CWR occurs. Figure 7 depicts the scenario for $Q = 10$ where time evolution of the dominant Fourier mode $W_{101}$ is displayed corresponding to different solutions that occur at different $r$. From Fig. 7, we notice that the 2D rolls as usual bifurcate into PWR through a supercritical Hopf bifurcation as $r$ increases [Figs. 7(a) and 7(b)]. Now, as $r$ is increased further, at $r = 1.7$ an inverse Hopf bifurcation takes place, and a transition from PWR to stable 2D rolls is observed. Further increment in $r$ brings back PWR ($2.07 \leqslant r \leqslant 2.4$) in the system before 2D rolls occur again in the window $2.4 < r < 2.88$. Near $r = 2.88$, transient chaos appears due to the presence of chaotic saddles in the system, and in a small interval ($2.88 \leqslant r \leqslant 2.89$) the transient chaos becomes persistent chaos with the increment in transient trapping time [Figs. 7(f)–7(h)]. The occurrence of different flow states for $Q = 10$ are also summarized in the line bifurcation diagram [Fig. 8(a)] as a function of $r$. Note that the scenario of transient chaos which eventually leads to persistent chaos appears in the system only for weak magnetic field, i.e., for $Q \leqslant 20$. For a moderate magnetic field ($20 < Q \leqslant 90$), the dynamics of the system changes qualitatively. Figure 8(b) highlights the transition to chaos for $Q = 50$. We observe the

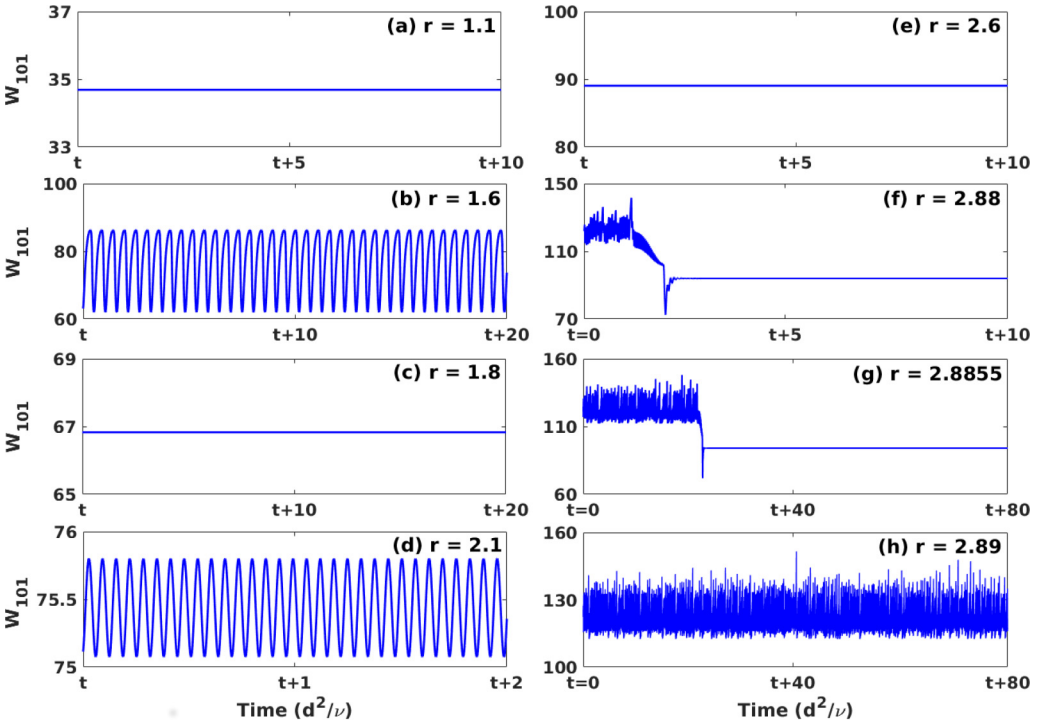


FIG. 7. Temporal evolution of the largest Fourier mode $W_{101}$ for $\Gamma = 4$ and $Q = 10$.

appearance of PWR windows in alteration with 2D rolls windows in this case too. However, the width of PWR regimes becomes smaller compared to that of $Q = 10$. This is found to be consistent with the property of the magnetic field when it acts in the horizontal direction, i.e., increment in the strength of the magnetic field suppresses the time-dependent solutions that appear near the onset of convection and postpones them to the higher $r$ [18]. At $r = 2.76$, the steady rolls become unstable through a supercritical Hopf bifurcation, and PWR appears in a very small window before QPWR is observed. The QPWR becomes chaotic at $r = 3.42$, and a standard quasiperiodic route to chaos is observed. For a stronger magnetic field ($Q > 90$), the PWR windows disappear from the system and the regime of SR extends [Fig. 8(c)]. The SR then goes through a Hopf bifurcation at $r = 1.923$,

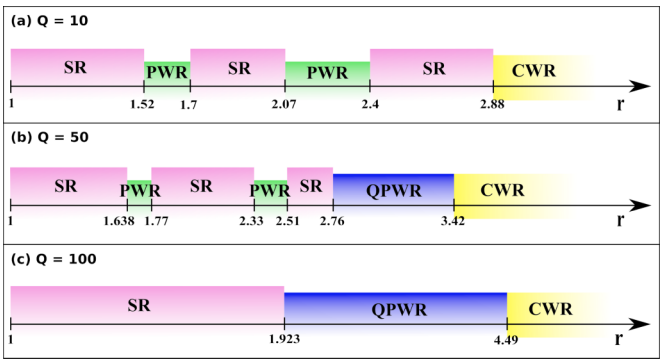


FIG. 8. (a–c) The line bifurcation diagrams constructed from DNS corresponding to $Q = 10$, $Q = 50$, and $Q = 100$, respectively, for $\Gamma = 4$. The color coding is same that has been used in Fig. 3.

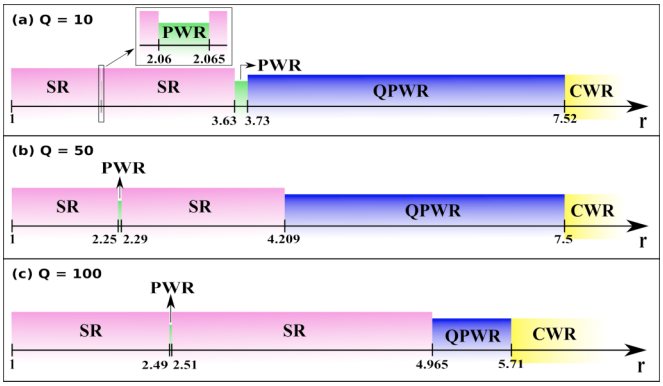


FIG. 9. (a–c) The line bifurcation diagrams constructed from DNS corresponding to $Q = 10$, $Q = 50$, and $Q = 100$, respectively, for $\Gamma = 6$. The color coding is same that has been used in Fig. 3.

and QPWR appears following the negligible appearance of PWR. At $r = 4.49$, CWR appears in the system, and a standard quasiperiodic route to chaos is observed in this case too.

### *4. Aspect ratio,* $\Gamma = 6$

Finally, we focus on $\Gamma = 6$. Only quasiperiodic route to chaos is preferred in the entire range of $Q$ ($0 < Q \leqslant 10^3$). The line bifurcation diagrams (Fig. 9) summarize the route to chaos corresponding to three different $Q$. We notice the appearance of a tiny PWR window between two successive SR windows for relatively lower $Q$ ($Q < 150$). Now, as $r$ is increased, the SR bifurcates into PWR via a supercritical Hopf bifurcation. The width of this PWR regime is found to be small corresponding to low $Q$ [Fig. 9(a)] and negligible for moderate and higher $Q$ [Figs. 9(b) and 9(c)]. Further increment in $r$ brings QPWR in the system before chaos is observed. Figure 10 displays the time series of $W_{101}$ corresponding to different flow states that occur at different $r$ for $Q = 10$. The presence of a quasiperiodic route to chaos (SR $\rightarrow$ PWR $\rightarrow$ SR $\rightarrow$ PWR $\rightarrow$ QPWR $\rightarrow$ CWR) is evident from

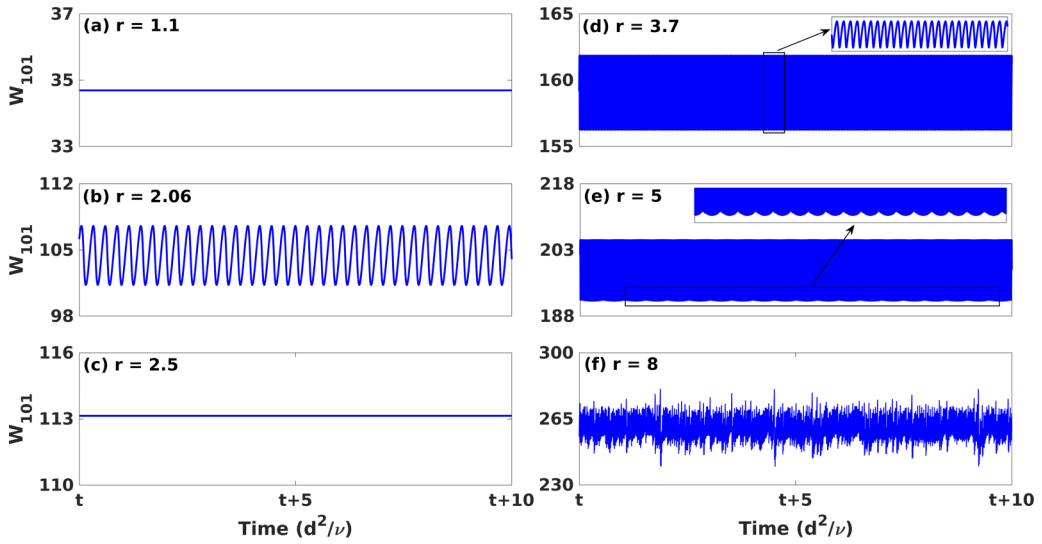


FIG. 10. Time series of the dominant Fourier mode $W_{101}$ illustrating quasiperiodic route to chaos for $\Gamma = 6$ and $Q = 10$. The insets in (d) and (e) show the enlarged view of the selected areas.

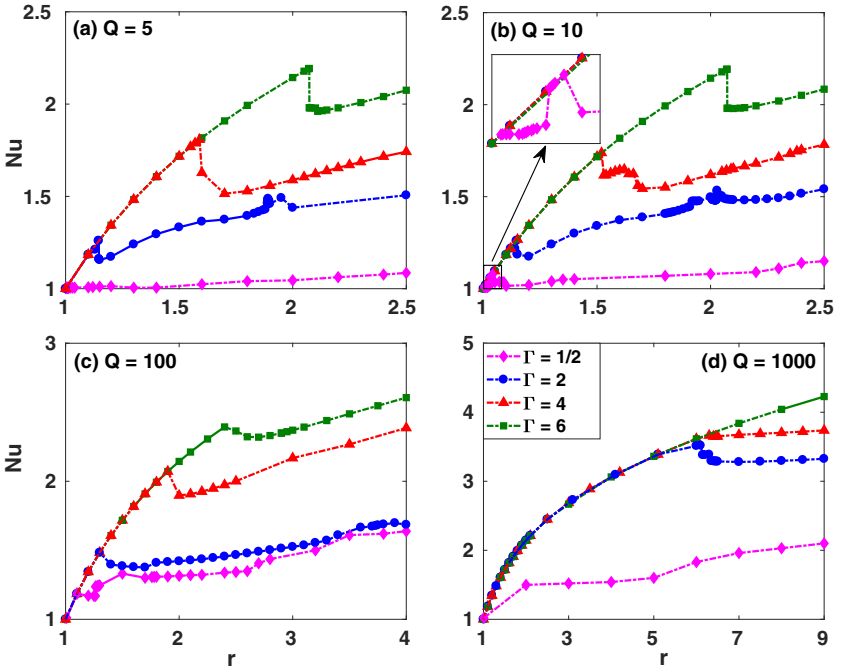


FIG. 11. Variation of Nu as a function r corresponding to four $Q$. Magenta diamonds, blue circles, red triangles, and green squares represent Nu corresponding to $\Gamma = 1/2$, 2, 4, and 6, respectively, as obtained from the DNS. The zoomed view of the selected area in (b) is shown at the inset.

Fig. 10. For a stronger magnetic field ($Q \geqslant 150$), the tiny PWR window occurring between two SR windows vanishes, and the SR regime extends. The SR then bifurcates into a tiny PWR regime which brings QPWR and CWR in the system, and a standard quasiperiodic route to chaos (SR $\rightarrow$ PWR $\rightarrow$ QPWR $\rightarrow$ CWR) is observed in this case too.

### C. Heat transport properties

Convective systems are often characterized by the changes occurring in global quantities such as the Nusselt number (Nu), which is the ratio of total heat flux (conductive and convective) to the conductive heat flux. In terms of nondimensional convective velocity and temperature, the definition of Nu reads as

$$\mathrm{Nu} = 1 + \mathrm{Pr}^2 \langle v_3 \theta \rangle^{xyzt}, \tag{11}$$

where $\langle \cdot \rangle$ represents the temporal and volume average of a specified quantity [40]. Therefore, in the conduction state Nu = 1, and it deviates from unity as convection sets in. From the discussion in Sec. IV B, it is evident that the physical system under consideration exhibits a diverse dynamics as the parameters $Q$ and $r$ are varied together with the system geometry $\Gamma$. Now, to uncover the heat transport properties associated with different solutions we construct four figures [Figs. 11(a)–11(d)] corresponding to four different $Q$ where Nu for different $\Gamma$ is displayed as a function of $r$.

From Fig. 11 we notice that for fixed $Q$ and $\Gamma$, Nu increases steadily in the SR flow regime with the increment in $r$. A diminution in Nu occurs as time-dependent solutions appear in the system. The diminution in Nu may be attributed to the extra dissipation caused by the toroidal component of motion, which does not contribute to the work of the buoyancy force [41]. Further increment in $r$ once again shows a steady increase in Nu. The effect of $Q$ on Nu is well known, i.e., increment

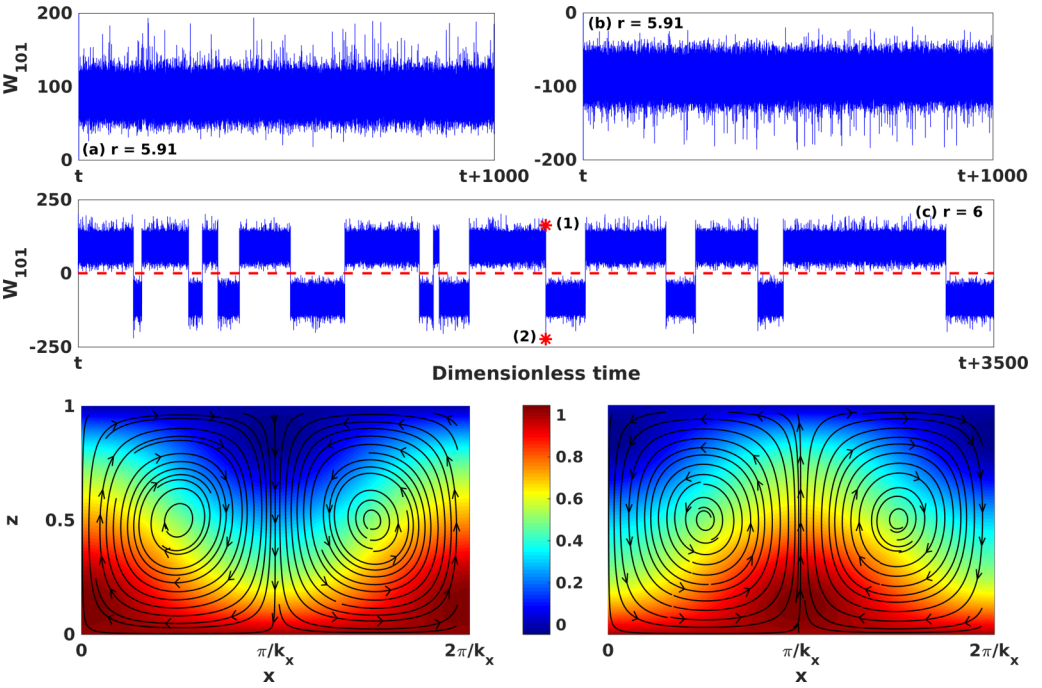


FIG. 12. Top two panels show the temporal evolution of the dominant Fourier mode $W_{101}$ for $\Gamma = 2$ and $Q = 100$: before the reversals (a, b) and after the reversals (c). The bottom panel displays the convective flow profile: before the reversals (left) and after the reversals (right) corresponding to the red stars (1) and (2) in (c), respectively.

in $Q$ enhances heat transport by increasing the regime of SR [17,19]. The present study reveals similar results (Fig. 11). However, the effect of $\Gamma$ on Nu for fixed $Q$ is found to be interesting as it also enhances heat transport by increasing the regime of SR (Fig. 11). Therefore, both $Q$ and $\Gamma$ are found to have a similar influence on the dynamics of the system.

### D. Flow reversals

Another interesting feature of low-Pr convection is flow reversal, which appears for relatively lower values of Ra [22]. Recently, Ghosh *et al.* [24] reported appearance of flow reversals near the onset of convection for $\Gamma = 1$ in the presence of an external horizontal magnetic field and showed that an attractor-merging crisis is responsible for that. Now, to uncover the effect of $\Gamma$ on flow reversals, we perform DNS with varying $\Gamma$ in our considered range. We find that flow reversals occur in the system for $\Gamma \leqslant 3$ only. The reversal mechanism is found to be similar to what has been reported by Ghosh *et al.* [24], i.e., attractor-merging crisis. The typical scenario of chaotic flow reversals occurring in the system is shown in Fig. 12 corresponding to $\Gamma = 2$ for $Q = 100$. Figures 12(a) and 12(b) display the time evolution of the dominant Fourier mode $W_{101}$ corresponding to two coexisting chaotic attractors connected through mirror symmetry of the system before reversals take place ($r = 5.91$). As the parameter $r$ crosses a critical value ($r_c = 5.92$), both chaotic attractors collide with the mediating unstable conduction state to form a single merged chaotic attractor and flow reversals set in. Figure 12(c) shows the time series of $W_{101}$ corresponding to the merged chaotic attractor for $r = 6$, while the bottom panel of Fig. 12 displays streamlines on top of isotherms for two consecutive instants (1) at $t = 1787.5$ (left) and (2) at $t = 1787.6$ (right) marked with red stars in Fig. 12(c). It is evident from Fig. 12 that as $W_{101}$ switches its sign the

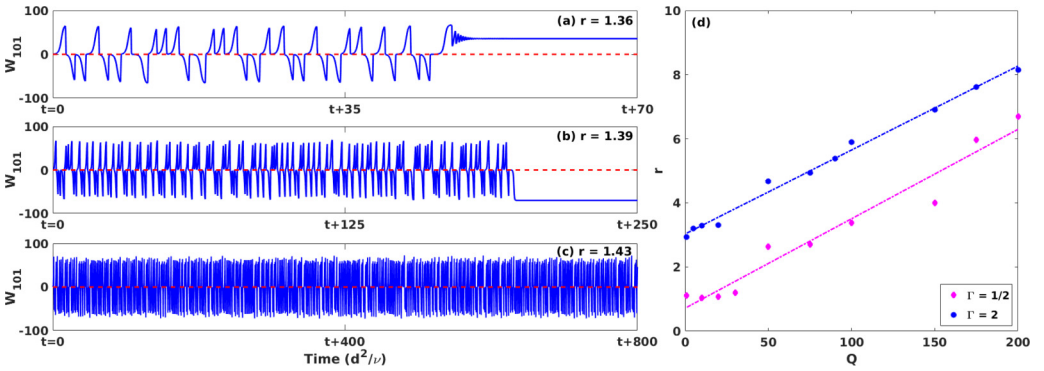


FIG. 13. (a–c) The transition to persistent chaotic flow reversals from transient chaotic flow reversals corresponding to $\Gamma = 1/2$ and $Q = 400$. (d) The onset of persistent flow reversals as a function of $Q$ for $\Gamma = 1/2$ (magenta diamonds) and $\Gamma = 2$ (blue circles), and the dash-dot lines denote their best linear fit.

direction of the velocity field reverses, indicating flow reversals. Note that we do not observe any roll-merging phenomena reported by Yanagisawa *et al.* [23] as our simulation box does not allow it [see ansatz (10)]. Also, we do not observe any periodic or intermittent reversals as observed by Mandal *et al.* [42] in the presence of a vertical magnetic field. However, variation in $\Gamma$ introduces diversity to the reversal dynamics, which is discussed below.

In Sec. IV B we have already shown that variation in $\Gamma$ reveals the presence of chaotic saddles or strange saddles in the system, which lead to the phenomenon of transient chaos. We have also noticed that the transient chaos may become persistent chaos with the increment in transient time as $r$ is increased gradually. The presence of transient chaos adds richness to the reversal dynamics and leads to the phenomena of transient chaotic flow reversals which further give rise to persistent chaotic flow reversals. The mechanism underlying transient chaotic flow reversals may be attributed to an attractor-merging crisis where two chaotic saddles connected via the system symmetry merge to form a merged chaotic saddle. This results in random transient reversals in the velocity field before stable patterns are observed. Figure 13(a) shows the presence of transient chaotic flow reversals in the system corresponding to $\Gamma = 1/2$ and $Q = 400$ in which time evolution of the largest Fourier mode $W_{101}$ is displayed for $r = 1.36$. From Fig. 13(a), we observe that $W_{101}$ switches sign randomly, indicating chaotic flow reversals before settling to the stable steady 2D rolls. Now, as we raise $r$ the transient time of the merged chaotic saddle increases [Fig. 13(b)], and finally we observe persistent merged chaotic attractor and persistent chaotic flow reversals [Fig. 13(c)]. The appearance of chaotic flow reversals directly from steady 2D rolls following the transient chaotic flow reversals is found to be quite fascinating, and we notice it in a widespread parameter space: $237 \leqslant Q \leqslant 1000$ for $\Gamma = 1/2$. It is interesting to mention that the transient chaos is also observed in the system for $\Gamma = 4$ corresponding to lower values of $Q$ (Fig. 7). However, for $\Gamma = 4$, the chaotic saddles never come closer to the mediating unstable conduction state as $r$ is varied. As a result, no attractor-merging phenomenon takes place, and we do not observe flow reversals.

Finally, we compute the onset of persistent flow reversals corresponding to different $Q$ ($0 < Q \leqslant 200$) for $\Gamma = 1/2$ and 2 to uncover the effect of the strength of the magnetic field on reversal dynamics. Figure 13(d) depicts the scenario where the appearance of persistent flow reversals is shown with magenta diamonds (blue circles) corresponding to different $Q$ for $\Gamma = 1/2$ ($\Gamma = 2$), while the magenta line (blue line) represents the best linear fit. From Fig. 13(d), it is evident that the phenomena of flow reversals are delayed as either $\Gamma$ or $Q$ increases. We identify that the critical value of $r$ corresponding to the flow reversals onset scales linearly with $Q$ in our considered parameter regime as $r = 0.0262Q + 3.0303$ for $\Gamma = 2$ and $r = 0.0279Q + 0.7135$ for $\Gamma = 1/2$.

## V. SUMMARY AND CONCLUSIONS

In summary, we have carried out extensive 3D DNS by varying the horizontal aspect ratio ($\Gamma = k_y/k_x$, where $k_x$ and $k_y$ are, respectively, the wave numbers along the $x$ and $y$ directions) of the simulation box to uncover its effect on the magnetoconvective instabilities using Rayleigh-Bénard geometry in the presence of an external uniform horizontal magnetic field. We focus on the dynamics of low-Prandtl number fluids (liquid metals) by varying the strength of the magnetic field (measured by the Chandrasekhar number, $Q$) in a widespread range $0 < Q \leqslant 10^3$. We have addressed different aspects of the problem including the oscillatory instability, transition to chaos, heat transport properties, and flow reversals. Several concluding remarks can be drawn from our detailed numerical investigation:

(i) The oscillatory instability onset is found to follow a well-defined law $(\mathrm{Ra_Q}^{(O)} - \mathrm{Ra_0}^{(O)}) \propto Q^{\alpha}$ [43]. However, depending on the strength of the magnetic field we identify two distinct scaling laws. For a weak and moderate magnetic field ($0 < Q < 100$), the exponent $\alpha$ is found to be higher compared to that of a stronger magnetic field ($100 \leqslant Q \leqslant 500$). Moreover, for a weak and moderate magnetic field, we find that $\alpha$ decreases with the increment in $\Gamma$ indicating enhancement of the steady roll regime. The Nusselt number (Nu) data obtained from DNS in this parameter regime also support this finding. In contrary, the oscillatory instability is absent for $\Gamma = 1/2$ corresponding to a stronger magnetic field, and we cannot draw any conclusion about its dependence on $\Gamma$ in this case.

(ii) We notice different routes to chaos depending on the strength of the magnetic field and $\Gamma$. The well-known period doubling route to chaos is observed for $\Gamma = 2$ corresponding to a weak magnetic field ($Q < 40$). Presence of weak intermittency is also observed there. On the other hand, a quasiperiodic route to chaos is preferred for $\Gamma = 1/2$ corresponding to a weak and moderate magnetic field ($Q \leqslant 130$), for $\Gamma = 2$ and 4 corresponding to a moderate and stronger magnetic field, and for $\Gamma = 6$ corresponding to an arbitrary magnetic field strength ($0 < Q \leqslant 10^3$). Note that, for $\Gamma = 1/2$ corresponding to a stronger magnetic field ($Q > 130$) and for $\Gamma = 4$ corresponding to a very weak magnetic field, we observe sharp transitions to chaos from steady 2D rolls due to the presence of transient chaos in the system.

(iii) The occurrence of transient chaos (TC) for $\Gamma = 1/2$ and 4 which eventually leads to persistent chaos is found to be a remarkable finding of the present study. The appearance of TC may be attributed to the presence of chaotic saddles or strange saddles in the system [38,44]. Note that TC has been reported earlier in low-dimensional models of magnetoconvection with finite magnetic Prandtl number (Pm) [21,37]. However, our study reveals that it is a possible route to chaos in quasistatic magnetoconvection ($\mathrm{Pm} \to 0$) when system geometry is varied.

(iv) Finally, we observe chaotic flow reversals in the system for $\Gamma \leqslant 3$ caused by an attractor-merging crisis [24]. The presence of TC adds richness to the reversals dynamics and leads to the phenomena of transient chaotic flow reversals for $\Gamma = 1/2$ where velocity field switches its direction randomly for finite time before converging to the steady 2D rolls. The appearance of transient chaotic flow reversals may be attributed to the presence of a merged chaotic saddle, formed due to the merging of two chaotic saddles (connected via mirror symmetry of the system). It is seen that the transient chaotic flow reversals eventually lead to persistent chaotic flow reversals with the increment in transient trapping time as $r$ is increased. The onset of persistent flow reversals is also found to follow a linear scaling with the strength of the magnetic field for different $\Gamma$.

Although we have addressed different aspects of magnetoconvection in the instability region by varying the horizontal aspect ratio of the simulation box, several questions are still unanswered and open for future investigation. For example, in a recent study, Mandal *et al.* [42] reported three different types of flow reversals, namely, periodic, intermittent, and chaotic, near the onset of convection in Rayleigh-Bénard convection in the presence of a vertical magnetic field. However, the effect of aspect ratio on these flow patterns and their origin are still unexplored. Also, the effect of an inclined magnetic field together with different magnetic boundary conditions is an interesting problem which deserves future attention.

**ACKNOWLEDGMENTS**

P.P. acknowledges the support from Science and Engineering Research Board (Department of Science and Technology, India) (Grant No. EMR/2015/001680). M.G. is grateful to the Science and Engineering Research Board (Department of Science and Technology, India) for support under NPDF (PDF/2020/000916). The authors thank A. Banerjee, S. Mandal, and S. Sarkar for their useful suggestions and fruitful comments.

[1] E. Priest, *Magnetohydrodynamics of the Sun* (Cambridge University Press, Cambridge, 2014).
[2] S. Stanley and G. A. Glatzmaier, Dynamo models for planets other than Earth, Space Sci. Rev. **152**, 617 (2010).
[3] A. Ribeiro, G. Fabre, J.-L. Guermond, and J. M. Aurnou, Canonical models of geophysical and astrophysical flows: Turbulent convection experiments in liquid metals, Metals **5**, 289 (2015).
[4] D. T. J. Hurle and R. W. Series, in *Handbook of Crystal Growth*, edited by D. T. J. Hurle (Elsevier, North Holland, Amsterdam, 1994).
[5] A. Gailitis, O. Lielausis, E. Platacis, G. Gerbeth, and F. Stefani, Colloquium: Laboratory experiments on hydromagnetic dynamos, Rev. Mod. Phys. **74**, 973 (2002).
[6] P. A. Davidson, X. He, and A. J. Lowe, Flow transitions in vacuum arc remelting, Mater. Sci. Technol. **16**, 699 (2000).
[7] E. Bodenschatz, W. Pesch, and G. Ahlers, Recent developments in Rayleigh-Bénard convection, Annu. Rev. Fluid Mech. **32**, 709 (2000).
[8] G. Ahlers, S. Grossmann, and D. Lohse, Heat transfer and large scale dynamics in turbulent Rayleigh-Bénard convection, Rev. Mod. Phys. **81**, 503 (2009).
[9] F. Chillà and J. Schumacher, New perspectives in turbulent Rayleigh-Bénard convection, Eur. Phys. J. E **35**, 58 (2012).
[10] S. Chandrasekhar, *Hydrodynamic and Hydromagnetic Stability* (Cambridge University Press, Cambridge, 1961).
[11] N. O. Weiss and M. R. E. Proctor, *Magnetoconvection* (Cambridge University Press, Cambridge, 2014).
[12] F. H. Busse and R. M. Clever, Stability of convection rolls in the presence of a horizontal magnetic field, J. Méc. Théor. Appl. **2**, 495 (1983).
[13] S. Fauve, C. Laroche, and A. Libchaber, Horizontal magnetic field and the oscillatory instability onset, J. Phys. Lett. **45**, 101 (1984).
[14] Y. Nandukumar and P. Pal, Oscillatory instability and routes to chaos in Rayleigh-Bénard convection: Effect of external magnetic field, Europhys. Lett. **112**, 24003 (2015).
[15] J. C. Yang, T. Vogt, and S. Eckert, Transition from steady to oscillating convection rolls in Rayleigh-Bénard convection under the influence of a horizontal magnetic field, Phys. Rev. Fluids **6**, 023502 (2021).
[16] F. H. Busse, The oscillatory instability of convection rolls in a low Prandtl number fluid, J. Fluid Mech. **52**, 97 (1972).
[17] S. Fauve, C. Laroche, and A. Libchaber, Effect of a horizontal magnetic field on convective instabilities in mercury, J. Phys. Lett. **42**, 455 (1981).
[18] P. Pal and K. Kumar, Role of uniform horizontal magnetic field on convective flow, Eur. Phys. J. B **85**, 201 (2012).
[19] U. Burr and U. Müller, Rayleigh-Bénard convection in liquid metal layers under the influence of a horizontal magnetic field, J. Fluid Mech. **453**, 345 (2002).
[20] A. Libchaber, S. Fauve, and C. Laroche, Two-parameter study of the routes to chaos, Physica D **7**, 73 (1983).
[21] W. M. Macek and M. Strumik, Hyperchaotic Intermittent Convection in a Magnetized Viscous Fluid, Phys. Rev. Lett. **112**, 074502 (2014).
[22] M. Mannattil, A. Pandey, M. K. Verma, and S. Chakraborty, On the applicability of low-dimensional models for convective flow reversals at extreme Prandtl numbers, Eur. Phys. J. B **90**, 259 (2017).

[23] T. Yanagisawa, Y. Yamagishi, Y. Hamano, Y. Tasaka, and Y. Takeda, Spontaneous flow reversals in Rayleigh-Bénard convection of a liquid metal, Phys. Rev. E **83**, 036307 (2011).
[24] M. Ghosh, A. Banerjee, and P. Pal, Crisis-induced flow reversals in magnetoconvection, Phys. Rev. E **104**, 015111 (2021).
[25] G. A. Glatzmaiers and P. H. Roberts, A three-dimensional self-consistent computer simulation of a geomagnetic field reversal, Nature (London) **377**, 203 (1995).
[26] T. Yanagisawa, Y. Hamano, and A. Sakuraba, Flow reversals in low-Prandtl-number Rayleigh-Bénard convection controlled by horizontal circulations, Phys. Rev. E **92**, 023018 (2015).
[27] A. V. Getling, *Rayleigh-Bénard Convection: Structures and Dynamics* (World Scientific, Singapore, 1998).
[28] O. Zikanov and A. Thess, Direct numerical simulation of forced MHD turbulence at low magnetic Reynolds number, J. Fluid Mech. **358**, 299 (1998).
[29] P. H. Roberts, *An Introduction to Magnetohydrodynamics* (Longmans, London, 1967).
[30] M. K. Verma, A. Chatterjee, K. S. Reddy, R. K. Yadav, S. Paul, M. Chandra, and R. Samtaney, Benchmarking and scaling studies of pseudospectral code Tarang for turbulence simulations, Pramana **81**, 617 (2013).
[31] K. Stork and U. Müller, Convection in boxes: Experiments, J. Fluid Mech. **54**, 599 (1972).
[32] R. Clever and F. Busse, Transition to time-dependent convection, J. Fluid Mech. **65**, 625 (1974).
[33] S. Fauve, E. W. Bolton, and M. E. Brachet, Nonlinear oscillatory convection: A quantitative phase dynamics approach, Physica D **29**, 202 (1987).
[34] S. Fauve, C. Laroche, A. Libchaber, and B. Perrin, Chaotic Phases and Magnetic Order in a Convective Fluid, Phys. Rev. Lett. **52**, 1774 (1984).
[35] A. Libchaber, C. Laroche, and S. Fauve, Period doubling cascade in mercury, a quantitative measurement, J. Phys. Lett. **43**, 211 (1982).
[36] C. Grebogi, E. Ott, and J. A. Yorke, Crises, sudden changes in chaotic attractors, and transient chaos, Physica D **7**, 181 (1983).
[37] F. F. Franco and E. L. Rempel, Chaotic saddles in a generalized Lorenz model of magnetoconvection, Int. J. Bifurcation Chaos **30**, 2030034 (2020).
[38] B. Eckhardt, T. M. Schneider, B. Hof, and J. Westerweel, Turbulence transition in pipe flow, Annu. Rev. Fluid Mech. **39**, 447 (2007).
[39] T. Tél, The joy of transient chaos, Chaos **25**, 097619 (2015).
[40] O. Thual, Zero-Prandtl-number convection, J. Fluid Mech. **240**, 229 (1992).
[41] R. M. Clever and F. H. Busse, Nonlinear oscillatory convection, J. Fluid Mech. **176**, 403 (1987).
[42] S. Mandal, M. Ghosh, A. Banerjee, and P. Pal, Dynamics of flow reversals in the presence of a vertical magnetic field, Europhys. Lett. **135**, 54005 (2021).
[43] F. H. Busse and J. A. Whitehead, Instabilities of convection rolls in a high Prandtl number fluid, J. Fluid Mech. **47**, 305 (1971).
[44] Y.-C. Lai and T. Tél, *Transient Chaos: Complex Dynamics on Finite Time Scales* (Springer Science & Business Media, 2011).